Computation of Aeolian Tones from Twin-Cylinders Using Immersed Surface Dipole Sources

Cheolung Cheong*
Professor, School of Mechanical Engineering, Pusan National University, 30, Jangjeon-dong, Geumjeong-gu, Pusan 609-745, Korea
Jewook Ryu
Ph. D, Gas Turbine Development Team, Center for Advanced Systems Development, Corporate R&D Institute, Doosan Heavy Industries & Construction Co. Ltd., 58-4 Hwaam-Dong, Yuseong-Gu, Daejeon 305-348, Korea
Soogab Lee
Professor, School of Mechanical and Aerospace Engineering, Seoul National University, Shinrim-dong, Gwanak-gu, Seoul 151-742, Korea

Efficient numerical method is developed for the prediction of aerodynamic noise generation and propagation in low Mach number flows such as aeolian tone noise. The proposed numerical method is based on acoustic/viscous splitting techniques of which acoustic solvers use simplified linearised Euler equations, full linearised Euler equations and nonlinear perturbation equations as acoustic governing equations. All of acoustic equations are forced with immersed surface dipole model which is developed for the efficient computation of aerodynamic noise generation and propagation in low Mach number flows in which dipole source, originating from unsteady pressure fluctuation on a solid surface, is known to be more efficient than quadrupole sources. Multi-scale overset grid technique is also utilized to resolve the complex geometries. Initially, aeolian tone from single cylinder is considered to examine the effects that the immersed surface dipole models combined with the different acoustic governing equations have on the overall accuracy of the method. Then, the current numerical method is applied to the simulation of the aeolian tones from twin cylinders aligned perpendicularly to the mean flow and separated 3 diameters between their centers. In this configuration, symmetric vortices are shed from twin cylinders, which leads to the anti-phase of the lift dipoles and the in-phase of the drag dipoles. Due to these phase differences, the directivity of the fluctuating pressure from the lift dipoles shows the comparable magnitude with that from the drag dipoles at 10 diameters apart from the origin. However, the directivity at 100 diameters shows that the lift-dipole originated noise has larger magnitude than, but still comparable to, that of the drag-dipole one. Comparison of the numerical results with and without mean flow effects on the acoustic wave emphasizes the effects of the sheared background flows around the cylinders on the propagating acoustic waves, which is not generally considered by the classic acoustic analogy methods. Through the comparison of the results using the immersed surface dipole models with those using point sources, it is demonstrated that the current methods can allow for the complex interactions between the acoustic wave and the solid wall and the effects of the mean flow on the acoustic waves.

Key Words : Computational Aeroacoustics, Tone Noise, Twin-Cylinder, Immersed Surface Dipole, Viscous/Acoustic Splitting Method

* Corresponding Author,
E-mail : ccheong@pusan.ac.kr
TEL : +82-51-510-2311; **FAX** : +82-51-514-7640
School of Mechanical Engineering, Pusan National University, 30, Jangjeon-dong, Geumjeong-gu, Pusan 609-745, Korea. (Manuscript **Received** May 27, 2006; **Revised** October 17, 2006)

Nomenclature

Roman Symbols

c : Speed of sound
C_d : Coefficient of drag
C_l : Coefficient of lift

D : Diameter of cylinder
e : total energy
e_0 : $e+1/2\cdot v^2$, stagnation total energy
h : Enthalpy
h_0 : $h+1/2\cdot v^2$, stagnation total enthalpy
I : Turbulence intensity
k : Turbulent kinetic energy
L : Turbulence length scale
ρ : Static pressure
P : $p-\lim_{T\to\infty}\int_{-T}^{T} pdt/T$, fluctuating surface pressure
Re : $u_\infty d/v$, Reynolds number
s : Entropy
$\boldsymbol{S}$: Immersed dipole source vectors
St : Df/u_∞, Strouhal number
T : Period of vortex shedding
t : Time
u_∞ : Free stream velocity
v_i : Fluid velocity in a cartesian coordinate system
x_i : Cartesian coordinate system

Greek symbols

γ : Ratio of specific heats, $\gamma=1.4$ for air.
ν : Kinetic viscosity
ν_t : Eddy viscosity
ν_{eff} : $\nu+\nu_t$, effective viscosity
ρ : Eensity
ε : Turbulence energy dissipation

Subscript

a : Denote the acoustical quantity
f : Denote the viscous flow quantity
∞ : Denote the free-stream quantity

1. Introduction

Aeolian tones from flow over cylinders are significant with airframe and power plant noise (tubular heat exchanger, power transmission lines and chimneys). Twin cylinders immersed in a stream are most fundamental configurations among other cylinder configurations. Zdravkovch (1977) classifies flow regimens in side-by-side and tandem arrangements for stationary cylinders as shown in Fig. 1. It is evident that various vortex shedding patterns from twin cylinders lead to their corresponding aeolian tone noises. There have been many experimental (Zdravkovich, 1977 and 1985; Kiya et al., 1980) or numerical investigations (Benhamadouche et al., 2003; Rollet-Miet et al., 1999; Bouris et al, 1999) on fluid dynamic characteristics of flows over cylinders. Some experimental works (Blevins and Ressler, 1983; Oengoren and Ziada, 1998), relevant to the noise from cylinders, have been done to understand the mechanism of flow-excited acoustic resonance in tubular heat exchanger. However, to the author's knowledge, any numerical works have not been done on the flow-induced noise from flow over multi-cylinders. The reason for this is because direct computation of the aerodynamic noise radiated by a subsonic flow where dipole noise sources are more effective than quadrupole types remains difficult because of the large computing resources, the expensive cost and physical/numerical issues (Tam, 1995; Lele, 1997) inherent in computational aeroacoustics (CAA).

The realization of these difficulties leads to the development of alternative methods, so-called hybrid methods. They involve separating the computation of the aerodynamic source term from that of the sound propagation. From a methodological point of view, the hybrid methods can be categorized into two types: One is semi-analytic method and the other is hybrid numerical method. The former utilizes integral formula derived from wave equations with source terms consisting of unsteady flow variables. Among the wave equation-type approaches, the most well-known is the wave equation formulated in Lighthill's acoustic analogy (Lighthill, 1952). Lighthill's acoustic analogy has been extended by Curle (1955) and Ffowcs Williams and Hawkings (1968) to allow for the effects of solid boundaries and their motion, respectively. In Lighthill's analogy, however, certain terms associated with the propagation of sound are treated as source terms. In practice, this limits the application of the theory to problems where mean flow effects on the wave propagation need not to be considered. The extended theories to account for the effects of solid boundaries are also based on the wave operator, similar to Lighthill's. Integral equations

require the Green function. In this regard, the application area is limited to cases in simple geometric configuration. The latter is based on the hybrid numerical method where the flow quantities are represented by their "base flow" components plus their "residual" components, which leads to two separate sets of equations governing viscous flow field and acoustic disturbance field, respectively. This approach is based on the assumption that the wave propagation is essentially inviscid in nature and sound perturbations are so small that their contribution to the convection velocity of the flow is negligible in most cases. The most significant advantage of the hybrid numerical mothod is that the best algorithms can be used for each solver : traditional CFD algorithms for the viscous flow and CAA algorithms for the acoustic perturbations. These separate solvers accommodate the disparate length scales (i.e., acoustic and convective) associated with low Mach number aeroacoustics. The convective length scales are resolved on a hydrodynamic grid, while the acoustic length scales are resolved on a separate acoustic grid. This merit makes the decomposition approaches cost-effective compared with the direct computational simulation (DNS) and large-eddy simulation (LES).

The hybrid numerical method for low-speed aeroacoustics, so-called the Expansion about Incompressible Flow (EIF), is mainly due to Hardin and Pope (1994 ; 1995). Their method utilizes information on the entire incompressible viscous flow field, which is obtained from the incompressible Navier-Stokes equations. Once a correction to the constant hydrodynamic density is obtained, acoustic radiation can be predicted from the compressible Euler equations in which the dependent variables are split into hydrodynamic terms and the acoustic terms. Shen and Sorensen (1999 ; 2001) found inconsistency in the previous formulation and proposed a new formulation. This new formulation was applied to laminar flows around a circular cylinder and turbulent flows past an airfoil. Recently, a set of perturbed compressible equations (Seo and Moon, 2005) was proposed to decouple the interaction effects between the incompressible vorticity and the perturbed velocities. The unphysical vorticity by these interactions is suppressed by introducing the perturbed viscous stress in the momentum equation.

In this paper, the acoustic/viscous splitting methods of which acoustic solver based on acoustic governing equations such as simplified linearized Euler equations, full linearized Euler equations and nonlinear perturbation equations, all of which are forced with immersed surface dipole model (ISDM), are utilized with emphasis placed on the prediction of aeolian tones from twin cylinders in a cross flow. The ISDM consists of point body forces immersed on each grid point on the solid surface. Their magnitudes are set by unsteady hydrodynamic pressure data deduced from the unsteady flow simulation using incompressible Computational Fluid Dynamics Techniques. Current method is applied to the cross flow past twin circular cylinders which are aligned perpendicularly to the free stream and are set to be 3 diameter distant between their centers. The choice of this configuration is because symmetric Karman vortex streets (anti phase vortex flow) are generated and resultant Aeolian tones are expected to be minimum compared to other configurations shown in Fig. 1 (Zdravkovich, 1985). It is very difficult to construct a single body-fitted mesh for twin cylinders which gives the proper resolution to both the near source region and far

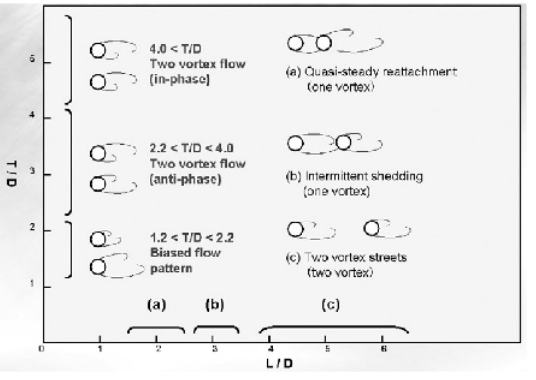

Fig. 1 Side-by-side and tandem configurations of twin cylinders and their corresponding vortex shedding patterns (From Zdravkovch, 1985)

acoustic field. The complex geometries and large disparate length scales are overcome by the use of a multi-scale overset grid technique, where body-fitted meshes are applied only near the cylinders and multi-scale Cartesian background mesh is applied elsewhere. Initially, aeolian tone from single cylinder is considered to examine the effects that the immersed surface dipole model, different acoustic governing equations and the interpolation between differing gird topologies have on the overall accuracy of the method. The validity of this hybrid approach is checked by comparing the numerical solution of single cylinder with the analytic solutions, which is obtained by using the two-dimensional point dipole solutions. Then, the characteristics of aeolian tones from twin cylinders in near- and far- field are assessed with a focus brought into the interactions between the acoustic wave and the solid body and the acoustic wave and the mean flow.

This article is composed of five sections. Section 2 presents the fundamental equations for the acoustic disturbance and the mathematical model for surface dipole source terms forcing the disturbance equations. The incompressible Navier-Stokes equations with the k-ε turbulence closure model for viscous flow fields are also reviewed. In Section 3, the numerical methods are presented for solving the acoustic and flow fields. Discretized model for the surface dipole source terms is also described. In Section 4, flow noise from the cross flow past a circular cylinder are investigated using the proposed methods. Detailed discussion on the numerical results is presented. In Section 5, aeolian tone noise due to a cross-flow over twin cylinders, aligned vertically to the mean flow and separated at distances of 3 diameters, are investigated. This result is also compared with the numerical solution using symmetric point dipole sources and other numerical results. Final section is devoted to the concluding remarks.

2. Fundamental Equations

2.1 Decomposed equations with source terms

The wave generation process is generally believed to be hardly affected by viscosity. We therefore begin with the unsteady Euler equations

$$\frac{\partial \rho}{\partial t}+\frac{\partial}{\partial x_j}\rho v_j=0 \tag{1}$$

$$\frac{\partial}{\partial t}\rho v_i+\frac{\partial}{\partial x_j}\rho v_i v_j+\frac{\partial p}{\partial x_i}=0 \tag{2}$$

$$\frac{\partial}{\partial t}\rho e_0+\frac{\partial}{\partial x_j}\rho h_o v_j=0 \tag{3}$$

The energy conservation equation (3) can be transformed to an equation for the pressure p by using the relation $(\partial e/\partial p)_s=p/\rho^2 c^2$.

$$\frac{\partial p}{\partial t}+v_j\frac{\partial p}{\partial x}+\gamma p\frac{\partial v_j}{\partial x_j}=0 \tag{4}$$

This equation (4) will be used instead of (3) because pressure is a quantity of great interest to acoustic problems. Sound perturbations are so small that their contribution to the convection velocity of the flow is negligible. This fact means that sound propagation is essentially described by using the variable decomposition methods. The dependent variables can be divided into their base flow components and into their residual components such that $\rho=\rho_0+\rho'$, $p=p_0+p'$, $v_i=v_{i,0}+v_i'$. Insertion of these decomposed variables to the Eqs. (1), (2) and (4) and subtraction of the resultant equations from the viscous flow equations satisfied by the base flow components lead to the governing equations for the residual components. It is evident that the different choice of the base flow variables leads to the different forms of acoustic governing equations (Goldstein, 2002).

If the base flow is a steady mean flow, the 2-D governing equations for the residual components are written as the following form

$$\frac{\partial \mathbf{U}}{\partial t}+\frac{\partial \mathbf{E}}{\partial x}+\frac{\partial \mathbf{F}}{\partial y}+\frac{\partial \mathbf{E}_{nl}}{\partial x}+\frac{\partial \mathbf{F}_{nl}}{\partial y}+\mathbf{H}=\mathbf{S} \tag{5}$$

where the unknown vector $\mathbf{U}$, the linear flux vectors $\mathbf{E}$ and $\mathbf{F}$, and the nonlinear flux vectors $\mathbf{E}_{nl}$ and $\mathbf{F}_{nl}$ are given by

$$\mathbf{U}=\begin{pmatrix}\rho'\\ \rho_0 u'\\ \rho_0 v'\\ p'\end{pmatrix},\ \mathbf{E}=\begin{pmatrix}\rho' u_0+\rho_0 u'\\ u_0\rho_0 u'+p'\\ u_0\rho_0 v'\\ u_0 p'+\gamma p_0 v'\end{pmatrix}\ \text{and}$$
$$\mathbf{F}=\begin{pmatrix}\rho' v_0+\rho_0 v u\\ v_0\rho_0 u'+p'\\ v_0\rho_0 v'\\ v_0 p'+\gamma p_0 v'\end{pmatrix} \tag{6}$$

$$\mathbf{E}_{\text{nl}}=\begin{pmatrix}\rho' u'\\ \rho_0 u'^2+2\rho' u' u_0+\rho' u'^2\\ \rho' u' v'+\rho' u' v_0+\rho' u_0 v+\rho_0 u' v'\\ p' u\end{pmatrix}$$

and (7)

$$\mathbf{F}_{\text{nl}}=\begin{pmatrix}\rho' v u\\ \rho' u' v'+\rho' u' v_0+\rho' u_0 v'+\rho_0 u' v'\\ \rho_0 v'^2+2\rho' v' v_0+p' v'^2\\ p' v'\end{pmatrix}$$

The vector $\mathbf{H}$ consists of mean flow gradient terms, which are equal to zero when mean flow is uniform :

$$\mathbf{H}=\begin{pmatrix}0\\ (\rho_0 u'+\rho' u_0)\dfrac{\partial u_0}{\partial x}+(\rho_0 v u+\rho' v_0)\dfrac{\partial u_0}{\partial y}\\ (\rho_0 u'+\rho' u_0)\dfrac{\partial v_0}{\partial x}+(\rho_0 v u+\rho' v_0)\dfrac{\partial v_0}{\partial y}\\ (\gamma-1)\left(\rho'\nabla\cdot\mathbf{u}_0-u'\dfrac{\partial p_0}{\partial x}-v'\dfrac{\partial p_0}{\partial y}\right)\end{pmatrix} \tag{8}$$

The vector $\mathbf{S}$ represents possible unsteady sources in the flow. For the efficient description of later numerical results, some terms are defined such that Nonlinear Perturbation Equations (NPE) denote the full equations of (6), Full Linearized Euler Equation (FLEE) represents Eqs. (6) without $\mathbf{F}_{nl}$ and $\mathbf{E}_{nl}$ and Simplified Linearized Euler Equations (SLEE) is defined as the Eqs. (6) without not only $\mathbf{F}_{nl}$ and $\mathbf{E}_{nl}$ but also $\mathbf{H}$.

2.2 Model for surface dipole sources

Assuming isentropic flows, noise generation is provided by source terms in the momentum equation of Eq. (5). In the present method, the source terms are modeled with the immersed surface dipoles of magnitude equal to the hydrodynamic unsteady pressure fluctuations on a solid surface.

First, let's introduce a function $f(x,t)$ where f is negative within the control surface, positive within the surrounding fluid and, also, f satisfies the equations $|\nabla f|=1$. Also, introduce a Heaviside function $H(x)$ defined as

$$H(x)=\begin{cases}1 \text{ for } x>0\\ 0 \text{ for } x<0\end{cases} \tag{9}$$

Then $H(f)$ vanishes within the control surface and is equal to unity in the region exterior to the surface. The gradient of the given fluctuating pressure in a solid body can be recast into the following form,

$$\begin{aligned}\nabla(p\cdot H(f)) &= H(f)\nabla P+P\nabla H(f)\\ &= H(f)\nabla P+P\nabla f\delta(f)\end{aligned} \tag{10}$$

where

$$P(\mathbf{x},t)=p(\mathbf{x},t)-p_0(\mathbf{x})$$

and

$$p_0(\mathbf{x})=\lim_{T\to\infty}\frac{1}{T}\int_{-T}^{T}p(\mathbf{x},t)\,dt$$

Then, in computation domain,

$$\nabla(p\cdot H(f))=P\nabla f\delta(f) \tag{11}$$

Then, the vector $\mathbf{S}$ is written as

$$\mathbf{S}=\begin{bmatrix}0\\ S_1\\ S_2\\ 0\end{bmatrix}=\begin{bmatrix}0\\ p\delta(f)\nabla f_1\\ p\delta(f)\nabla f_2\\ 0\end{bmatrix} \tag{12}$$

Data provided by incompressible or compressible simulations can be used to estimate S_i.

2.3 Governing equations for viscous flows

Present approach is focused on low Mach number flows where noise from dipole sources is generally dominant. The 2-D incompressible Reynolds-Averaged Navier-Stokes (RANS) equations therefore are used as the governing equations for viscous flow :

$$\frac{\partial u}{\partial x}+\frac{\partial v}{\partial y}=0 \tag{13}$$

$$\frac{\partial u}{\partial t}+u\frac{\partial u}{\partial x}+v\frac{\partial u}{\partial y} =-\frac{1}{\rho}\frac{\partial p}{\partial x}+\nu_{eff}\left(\frac{\partial^2 u}{\partial x^2}+\frac{\partial^2 u}{\partial y^2}\right) \tag{14}$$

$$\frac{\partial v}{\partial t}+u\frac{\partial v}{\partial x}+v\frac{\partial v}{\partial y} =-\frac{1}{\rho}\frac{\partial p}{\partial y}+\nu_{eff}\left(\frac{\partial^2 v}{\partial x^2}+\frac{\partial^2 v}{\partial y^2}\right) \tag{15}$$

where $\nu_{eff}=\nu+\nu_t$, and the eddy viscosity ν_t is modeled using the low Reynolds number k-ε turbulence model by Chien (1982). The eddy viscosity ν_t is given by

$$\nu_t=c_\mu f_\mu\frac{k^2}{\varepsilon} \tag{16}$$

where f_μ is defined as $f_\mu=1-e^{-0.0115u_* y/\nu}$ where u_* is the friction velocity and y is the normal distance from the wall. Two equations are involved in this turbulence model; one for k and another for ε as follows:

$$\frac{\partial k}{\partial t}+\frac{\partial u_j k}{\partial x_j}=\frac{1}{\rho}\frac{\partial}{\partial x_j}\left[\left(\mu+\frac{\mu_t}{\sigma_k}\right)\frac{\partial k}{\partial x_j}\right] +\mu_t\left(\frac{\partial u_i}{\partial x_j}+\frac{\partial u_j}{\partial x_i}\right)\frac{\partial u_j}{\partial x_i} -k\left(f_\mu C_\mu\rho\frac{k}{\mu_t}+\frac{2\mu}{y^2}\right) \tag{17}$$

$$\frac{\partial \varepsilon}{\partial t}+\frac{\partial u_j \varepsilon}{\partial x_j}=\frac{1}{\rho}\frac{\partial}{\partial x_j}\left[\left(\mu+\frac{\mu_t}{\sigma_\varepsilon}\right)\frac{\partial k}{\partial x_j}\right] +f_1 C_{\varepsilon 1}\mu_t\left(\frac{\partial u_i}{\partial x_j}+\frac{\partial u_j}{\partial x_i}\right)\frac{\partial u_j}{\partial x_i} -C_{\varepsilon 2}f_2\frac{\varepsilon^2}{k}-2\varepsilon\nu\frac{e^{-0.5y^+}}{y^2} \tag{18}$$

The empirical low-Reynolds number functions f_1 and f_2 appearing in the ε-equation (18) given by:

$$f_1=1.0,\ f_2=1-0.22\exp\left[(R_T/6)^2\right] \tag{19}$$

where $R_T=k^2/\nu\varepsilon$. The remaining empirical constants were allocated the following standard values cited by Chien: $C_\mu=0.09$, $C_{\varepsilon 1}=1.35$, $C_{\varepsilon 2}=1.80$, $\sigma_k=1.0$, and $\sigma_k=1.30$.

3. Numerical Methods

3.1 Numerical methods for acoustic solvers

The Cartesian coordinate system employed in Eq. (5) is inconvenient for solving problems which include curvilinear boundary lines. Thus, the spatial derivatives expressed as functions of the coordinates (x, y) need to be recast as functions of the curvilinear coordinates (ξ, η) by a general coordinate transformation. Accordingly, Eq. (5) in a physical domain is expressed by the coordinate variables in a computational domain. All the variables are non-dimensionalized with the following scales: D (diameter of cylinder) for the length scale, c_∞ for the velocity scale, D/c_∞ for the time scale, ρ_∞ for the density scale and $\rho_\infty c_\infty^2$ for the pressure scale, where c_∞ is the ambient speed of sound. The 7-point stencil, Grid-Optimized Dispersion-Relation-Preserving (GODRP) of Cheong and Lee (2001) was utilized to compute the spatial flux derivatives. Time integration is performed with the low-dissipation and low-dispersion Runge-Kutta schemes introduced by Hu et al. (1996). The radiation and outflow boundary conditions (Bayliss and Turkel, 1982), based on the asymptotic expressions for the three characteristic waves of Euler's equations in the far field, are implemented across the out-flow boundaries. The ghost value of pressure (Tam and Dong, 1994) was used as the extraneous hard wall boundary condition.

3.2 Numerical model for immersed surface dipole sources

The very act of discretization brings with it many numerical artifacts. The modeling of a delta function in an analytic expression for immersed surface dipole sources in Eq. (12) is necessary for a discrete numerical simulation. The delta function is modeled as

$$\delta(\mathbf{x})\cong\left(\frac{\ln 2}{\pi\sigma^2}\right)^{\frac{n}{2}}\exp(-\ln 2\cdot\mathbf{x}^2/\sigma^2) \tag{20}$$

where n (=1 or 2 or 3) denotes the dimension of delta function. Both sides of Eq. (20) satisfy the following space integral equation.

$$\int_{-\infty}^{\infty}\delta(\mathbf{x})\,d\mathbf{x} = \int_{-\infty}^{\infty}\left(\frac{\ln 2}{\pi\sigma^2}\right)^{\frac{n}{2}}\exp(-\ln 2\cdot\mathbf{x}^2/\sigma^2)\,d\mathbf{x}=1 \tag{21}$$

Although Eq. (21) guarantees the conservation of total energy of the delta function, i.e., the acoustic sources, there is still some differences in the distribution of functions of Eq. (20). It is evident that, as the value of σ is decreased, approximate formula of Eq. (20) yields more accurate results for the delta function. Combining Eqs. (21) and (12), the immersed surface dipole model in the two-dimension can be expressed as

$$S_i(\mathbf{x},t) = P(\mathbf{x},t)\cdot\left(\frac{\ln 2}{\pi\sigma^2}\right)\exp(-\ln 2\cdot f(\mathbf{x},t)^2/\sigma^2)\nabla f_i(\mathbf{x},t) \tag{22}$$

When a solid body occupies some portion of the immersed surface dipole sources, Eq. (22) needs to be slightly modified because Eq. (21) cannot be satisfied in a fluid region. Therefore, the correction factor, C is incorporated to Eq. (22) as follows

$$S_i(\mathbf{x},t) = P(\mathbf{x},t)\cdot C\cdot\left(\frac{\ln 2}{\pi\sigma^2}\right)\exp(-\ln 2\cdot f(\mathbf{x},t)^2/\sigma^2)\nabla f_i(\mathbf{x},t) \tag{23}$$

where

$$C=1\Big/\left(\int_{-\infty}^{\infty}\int_{-\infty}^{\infty}\left(\frac{\ln 2}{\pi\sigma^2}\right)\exp(-\ln 2\cdot\mathbf{x}^2/\sigma^2)\,dx_1dx_2 - \int_S\left(\frac{\ln 2}{\pi\sigma^2}\right)\exp(-\ln 2\cdot\mathbf{x}^2/\sigma^2)\,dx_1dx_2\right)$$

and S denotes the area of loss region of the immersed surface dipole sources due to the solid body.

3.3 Numerical methods for viscous flow simulations

The numerical method used for performing the viscous flow field prediction is based on the unstructured grid, finite volume method, presented in detail by Kang et al.(1998). The scheme has extended the unstructured grid Navier-Stokes procedure of Thomadakis et al.(1996) for incompressible flows to allow the collocated storage of all variables. Since Thomadakis et al. (1996) used a staggered-grid formulation, pressure data could be stored at the centroid of a cell while velocity components were stored at grid points. However, the scheme has been modified so that this procedure can employ collocated storage (non-staggered) to obviate the difficulties and disadvantages of implementing a non-collocated (staggered) mesh within the unstructured methodology.

The algebraic equation for hydrodynamic pressure was derived by substituting the discretized momentum equations into the continuity equation (Hobson and Lakshiminarayana, 1991). The process of deriving the pressure equation is almost the same as one used for a structured grid method. To retain second order accuracy of space and time discretization, the numerical method uses the Quadratic Upstream Interpolation for Convective Kinematics (QUICK) scheme for the convective terms and the second order Euler backward difference for time derivatives to keep second order accuracy in terms of space and time. All other spatial derivatives are approximated by the central difference schemes.

4. Numerical Results for Aeolian Tones from Single Cylinders

One of the advantages of the current approach is that it is able to capture the disparate length scales linked with low-Mach number flow-induced noise, where the acoustic wavelength is typically M^{-1} times longer than the flow length scale. The smaller convective length scales are resolved on an aerodynamic grid, while the acoustic length scales are resolved on a separated acoustic grid. Accordingly, the computed mean-flow and acoustic source data must be transformed from the grid and time-steps used for the flow-simulation into the grid and time-steps used for the acoustic simulation.

The numerical approach described above was applied to the prediction of aeolian tone noise from a two-dimensional cylinder flow. The Reynolds number, $Re=u_\infty D/\nu$, is equal to 1.58×10^4. These conditions were chosen to meet the general flow conditions in typical tubular heat exchangers and to coincide with existing experimental data of

the flow dynamics presented by Kiya et al. (1980) and Cantwell et al. (1983).

4.1 Numerical results of viscous flow simulations

The flow calculations were carried out on a mesh with approximately 20,000 grid points. The mesh with its close-up around the cylinder is shown in Fig. 2. The mesh for performing viscous flow simulation consists of two types grids: an inner mesh consisting of a multiply connected grid and an outer Cartesian grid. The inner mesh size was increased according to the distance from the cylinder surface, and the distance of the first grid point from cylinder surface is chosen to be 0.04% of the cylinder diameter (of the order of $\Delta y^+=1$) to ensure adequate spatial resolution in the laminar sub-layer.

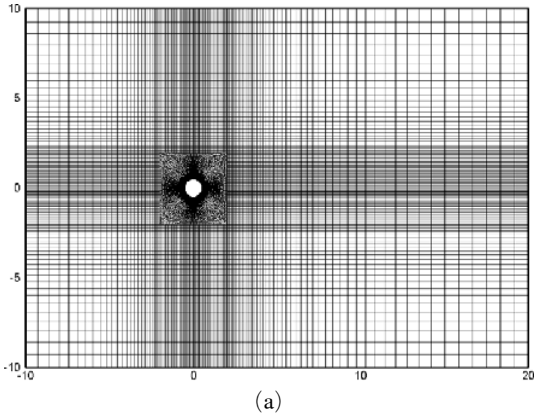

(a)

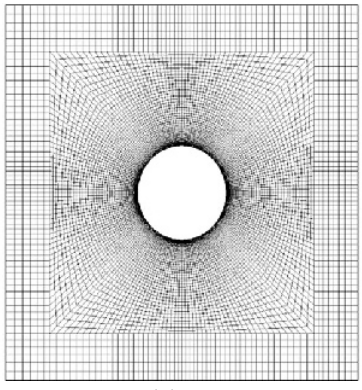

(b)

Fig. 2 The computational mesh used for viscous flow simulation; (a) Global domain grids and (b) the grids near the cylinder surface

Dirichlet boundary conditions are used at the far field boundaries as well as at the cylinder surface. The convective boundary conditions were used as the outflow boundary condition in order to smoothly pass vortices waves from the computational domain. In addition to the initial flow condition and the boundary conditions for the velocity, the free stream inlet turbulence values for the kinetic energy $k=3/2(I_u u_\infty)^2$ and the turbulence dissipation $\varepsilon=10C_\mu k^{3/2}/L_x$ have been imposed corresponding to a turbulence intensity (I_u) of 0.6% and a non-dimensional turbulence length scale (L_x/D) of 0.02 for the k-ε based turbulence model. Initially, random disturbances were imposed on the uniform velocity field to ensure that vortex shedding occurs quickly. The computational time step was fixed as $\Delta t=0.01$ (D/u_∞).

Lift and drag forces exerted on the cylinder surface fluctuate in time due to the periodic shedding of vortices. The frequency or period of vortex shedding can be estimated by evaluating those of the oscillating lift or drag coefficient. Time-dependent lift and drag coefficients are presented in Fig. 3, calculated by integrating the distributions of pressure and shear stresses on the cylinder surface. Although the computation begins from an initial condition with randomly imposed

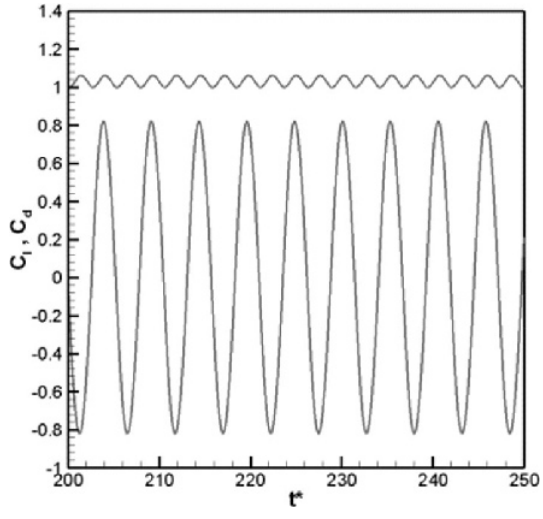

Fig. 3 Time-dependent signals of lift (lower) and drag (upper) coefficients

disturbances, vortex shedding does not occur until a non-dimensional time $t_f=180$. However, once the first shedding occurs, the flow solution passes through a transient interval to reach steady state where vortices are shed periodically. Lift and drag coefficients exhibit a sinusoidal time variation corresponding to a Strouhal number of 0.192 and 0.384, respectively. This value is in good agreement with the experimental measurement (Kiya et al., 1980). It is noted that the drags oscillate at twice the Strouhal number corresponding to the fluctuating lift.

Figure 4 shows a comparison between the measured and predicted time-averaged drag coefficient and vortex-shedding Strouhal number with experimental data (Cantwell and Coles, 1983).

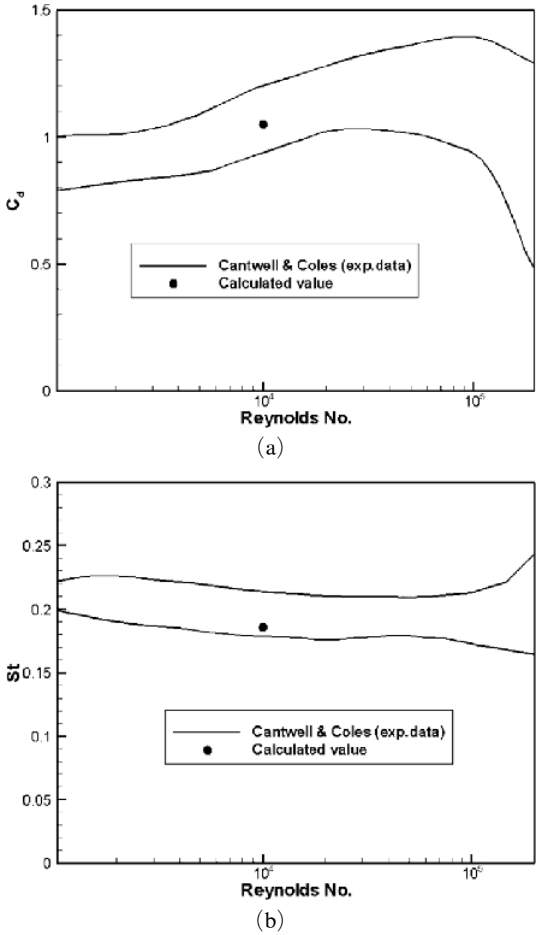

Fig. 4 Comparisons of calculated $\overline{C}_d$ and S_t with experiment; (a) $\overline{C}_d$ vs. Re and (b) St vs. Re

The upper and lower curves in represent the variability in the experimental data collected by Cantwell and Coles. Reasonable agreement is observed at the Reynolds number $Re=1.58\times10^4$ of the simulation.

4.2 Numerical results of acoustic simulations

Hydrodynamic unsteady data obtained from the viscous flow simulation using incompressible RANS are now used to build up the source terms of Eqs. (12) and (23). The dipole source terms of Eqs. (12) and (23) were computed at every iteration within a single vortex shedding period on a solid surface. Non-dimensional period T_f of the vortex shedding is equal to 5.2 with $\Delta t_f=0.01$, which correspond to 520 data points in time. Unsteady hydrodynamic pressure corresponding to a surface dipole source is recorded on a cylinder surface consisting of 101 grid points. Physical time is non-dimensionalized by D/u_∞ in the viscous flow simulation, and by D/c_∞ in the acoustic simulation. The different time-scales in the acoustic simulation and the viscous flow simu-

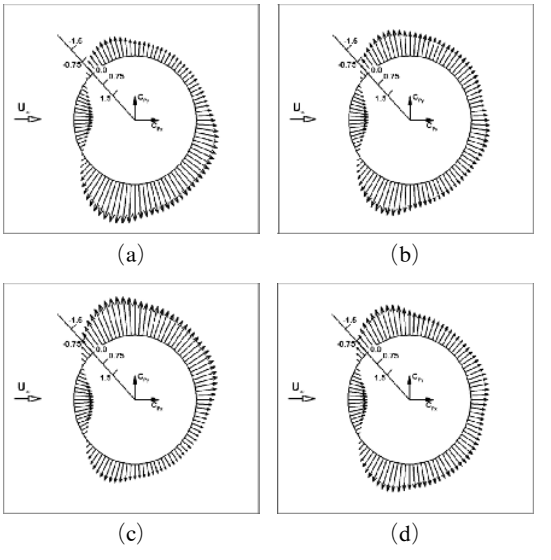

Fig. 5 A sequence of simultaneous surface pressure coefficients ($Cp=0.5(p-p_\infty)/pv_\infty^2$) at (a) one quarter of a cycle, (b) a half cycle, (c) three quarters of a cycle, (d) the beginning of a cycle

lations lead to the different non-dimension period of T_a=72.25 and numerical time step of Δt_a= 0.02, i.e. 3614 data points to represent one period of oscillation. Furthermore, the mesh for the acoustic calculation is the O-type grid which extends to the far-field reaching to $100D$ in this computation. Thus, the domain includes both the near field and the far field.

The numerical results of the viscous flow are transformed onto the grid and the time step for acoustics simulation. Figures 5 and 6 show the hydrodynamic pressure p and fluctuating pressure P on the cylinder surface at approximately $0.25\,T_a$, $0.5\,T_a$, $0.75\,T_a$ and T_a, respectively. Fluctuating pressure data are utilized as input data for the construction of the immersed surface dipole sources.

Acoustic computations are carried out with the O-type meshes consisting of the 101×998 grid points in ξ- and η-directions, respectively. Acoustic calculations were first executed without mean flow, i.e. with only the modeled source terms. Then acoustic calculations are carried out with three CAA solvers respectively based on the SLEE, FLEE, and NPE forced with the ISDM.

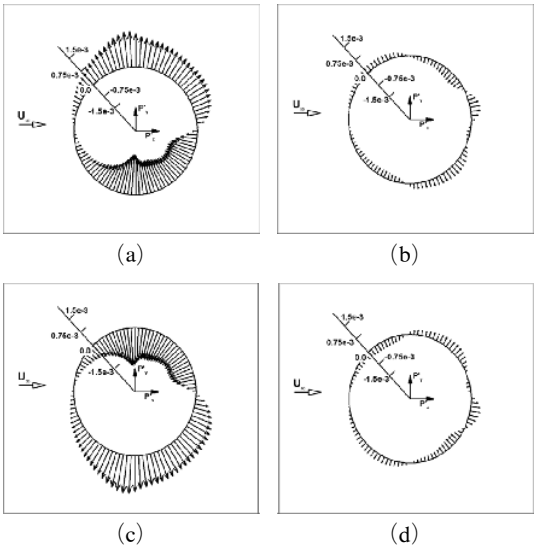

(a) (b) (c) (d)

Fig. 6 A sequence of simultaneous surface fluctuating pressure (P) at (a) one quarter of a cycle, (b) a half cycle, (c) three quarters of a cycle, (d) the beginning of a cycle

4.2.1 Acoustic results without mean flow effects

In Fig. 7, fluctuating pressure field obtained from the simulation using the ISDM in ambient condition is plotted at nondimensional time instant T=250. As expected, the acoustic wave is seen to be mainly propagated in the direction normal to the freestream velocity. Fig. 7(b) shows

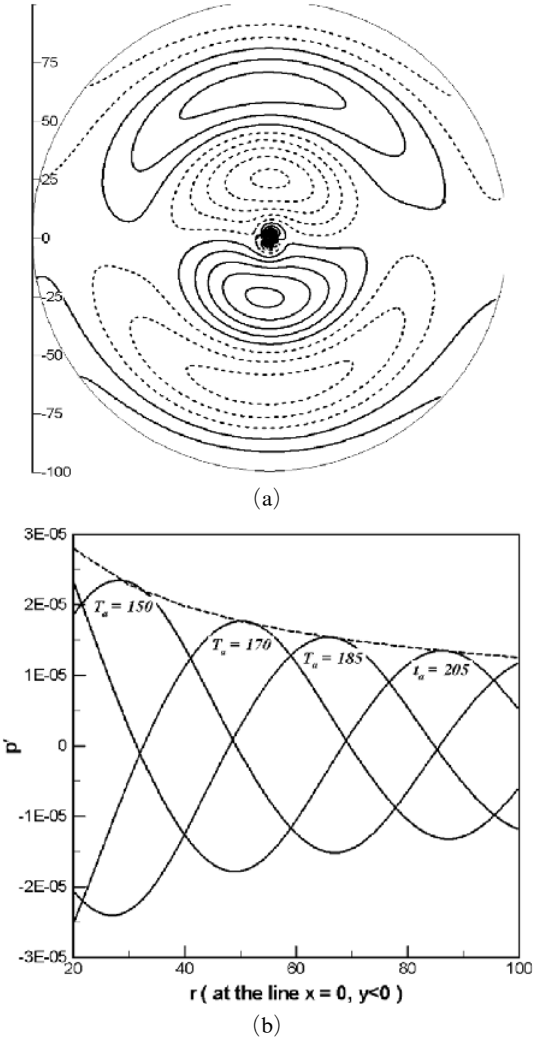

(a) (b)

Fig. 7 Instantaneous fluctuating pressure distribution; (a) pressure contours with 120 levels from −3.1e-4 to 3.1e-4 and (b) pressure distribution along the y-axis ($y<0$): —— numerical results, ---- decay lines correspond to $c/r^{0.5}$ where c is the value of pressure at r=50 in the lines of T_a=170

the pressure waveform along the y-axis ($y<0$) at various time instants. The dashed line is directly proportional to $y^{-0.5}$ and can be seen to correspond to the envelope of the pressure distribution along the y-axis, as is characteristic of the cylindrical decay of two-dimensional sound fields.

The time history of the fluctuating pressure, predicted at a distance $r=99D$ from the cylinder center, is shown in Fig. 8 at the four circumferential positions of $\theta=0°$, 90°, 180° and 270°, which are measured from the x-axis in a counter-clock wise direction. The time signals pass through a transient state to arrive at a state of steady periodicity. It is observed that the pressure signals at $\theta=90°$ and 270° are dominated by signals oscillating at the strouhal frequency, and the signals at 0° and 180° by signals oscillating at twice the strouhal frequency. This is a physically plausible result because the lift dipole is dominant at the strouhal frequency and the drag dipole is dominant at twice the strouhal frequency.

The directivity pattern of the sound field in the current example, measured at a distance $r=99D$ from the cylinder center, is shown in Fig. 9. Numerical results are compared with the analytic solution (Blake, 1986). Numerical result shows good agreement with analytic solution.

4.2.2 Acoustic results with the LEE

The SLEE and FLEE combined with the ISDM are utilized for the acoustic simulations. The SLEE is proposed to prevent the exponenti-

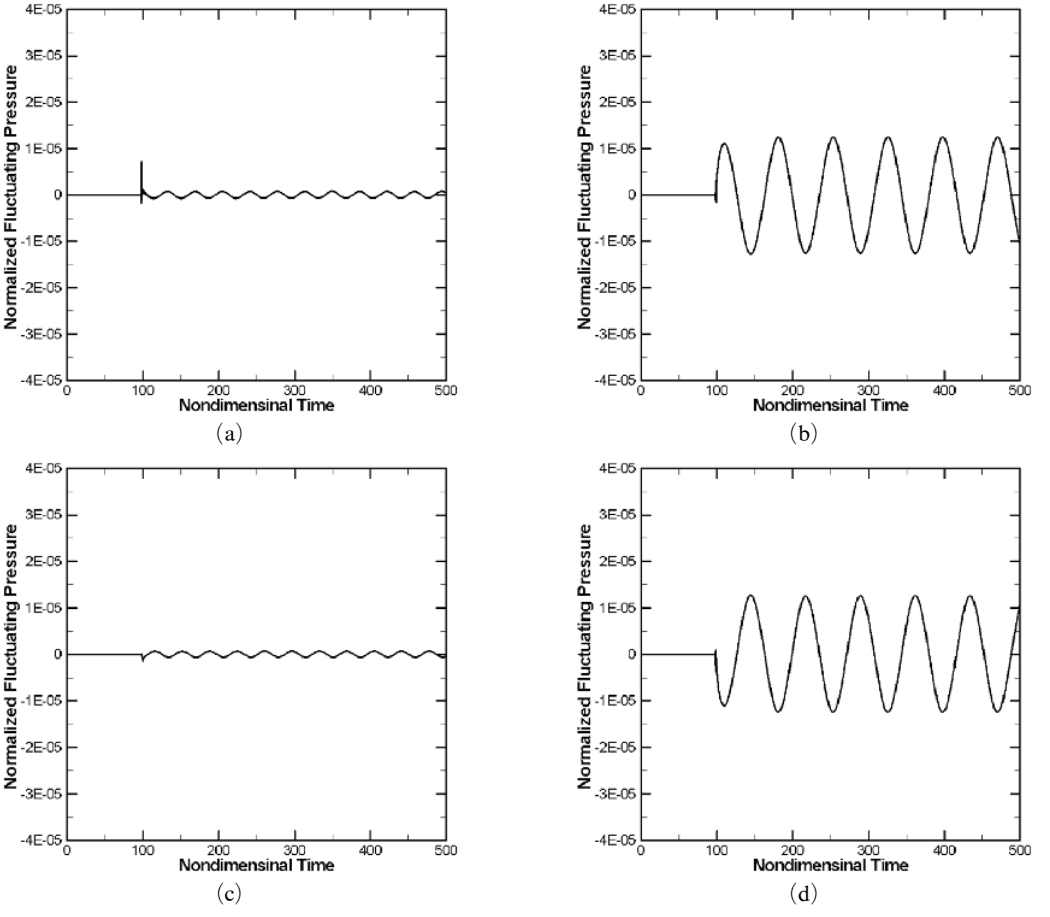

Fig. 8 Fluctuating pressure signal from the ISDM without mean-flow at $r=99D$ measured at (a) $\theta=0°$, (b) $\theta=90°$, (c) $\theta=180°$, and (d) $\theta=270°$

al growth of instability waves by Bogey et al. (2002).

Figure 10 shows vorticity contours around the cylinder for each time instant. We can see that vortices are periodically shed from the cylinder at the strouhal frequency. These vortices are generated by the immersed surface dipole sources and solid boundary condition. Without mean flow, vorticities cannot move downward from a cylinder while, with mean flow, the vorticities can do at the same speed of the mean flow. This convection, therefore, makes it possible to continuously transport the energy from acoustic wave to the vorticity wave. This process leads to the decrease of the amplitude in the fluctuation pressure for using the ISDM with mean flow. Real physical noise generation mechanism on Aeolian tone from a cylinder can be understood as the transformation of the energy of vorticity waves into acoustical energy on solid surface. Because the immersed surface dipoles just model the resultant acoustic dipole sources without describing the origin of acoustic energy, unphysical phenomena appear in the numerical simulations. However, if the main concern of the acoustic simulation is the propagating acoustic wave in the far field. The ISDM provides sufficient information for this purpose only if the

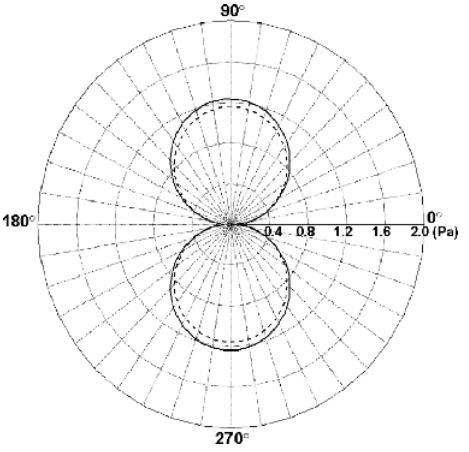

Fig. 9 Directivity patterns of the RMS value of the fluctuating pressure at $r=99D$: —— numerical results by using the ISDM without mean flow effects, ---- analytic results

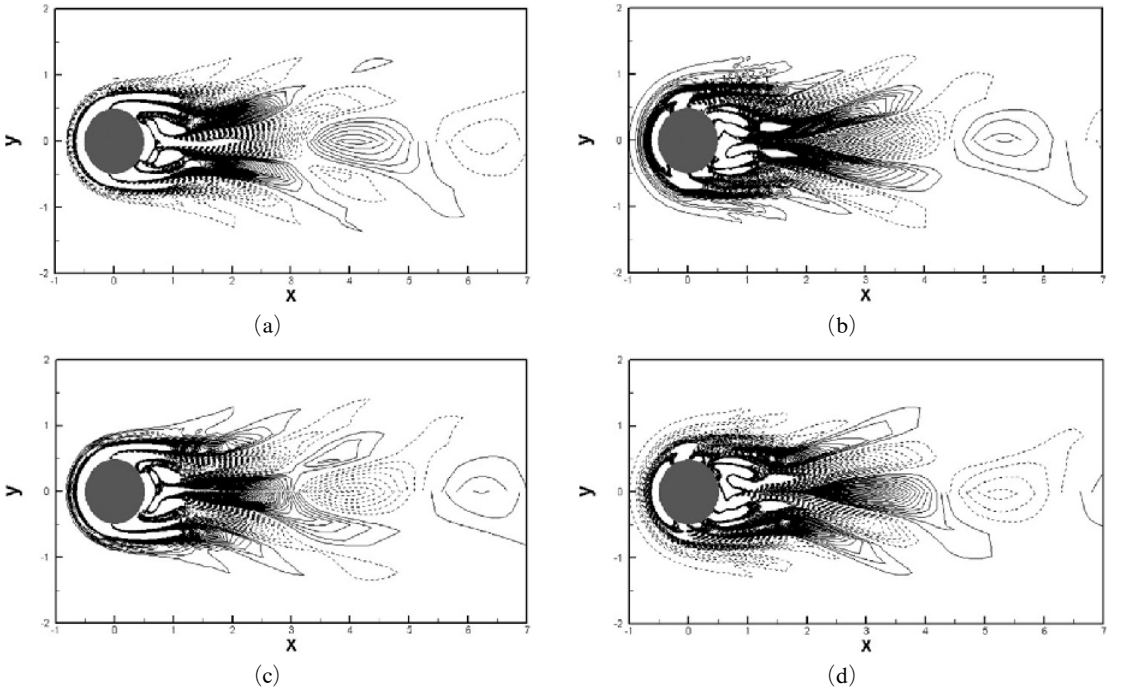

Fig. 10 Vorticity contours from the ISDM combined with the SLEE : 80 levels from −5.e-2 to 5.e-2 and —— positive value, ---- negative values. (a) $T=430$, (b) $T=450$, (c) $T=465$ and (d) $T=485$

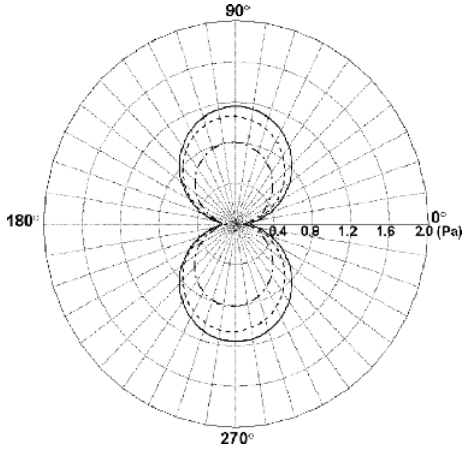

Fig. 11 Directivity patterns of the RMS value of the fluctuating pressure at $r=99D$: —— Analytic Sol., - - - - Slightly Distant ISDM, and : -·-·-·- the original ISDM

transferred energy is reduced. In order to suppress the transported energy, the surface dipole sources are immersed at the locations slightly distant from the surface wall instead of being set on the surface grid points. The sources slightly apart from the solid wall decrease the amount of the transported energy from the acoustic wave to the vorticity wave and, as a result, diminish the difference between the amplitudes in the oscillating pressures using the ISDM with and without mean flow.

Figure 11 presents the comparison of the directivity obtained by using the modified ISDM and the original ISDM. All of the immersed surface dipole sources of the modified ISDM are moved off the solid wall to be $0.1D$ distant from the cylinder surface. It can be found that the solution from the slightly distant sources shows a

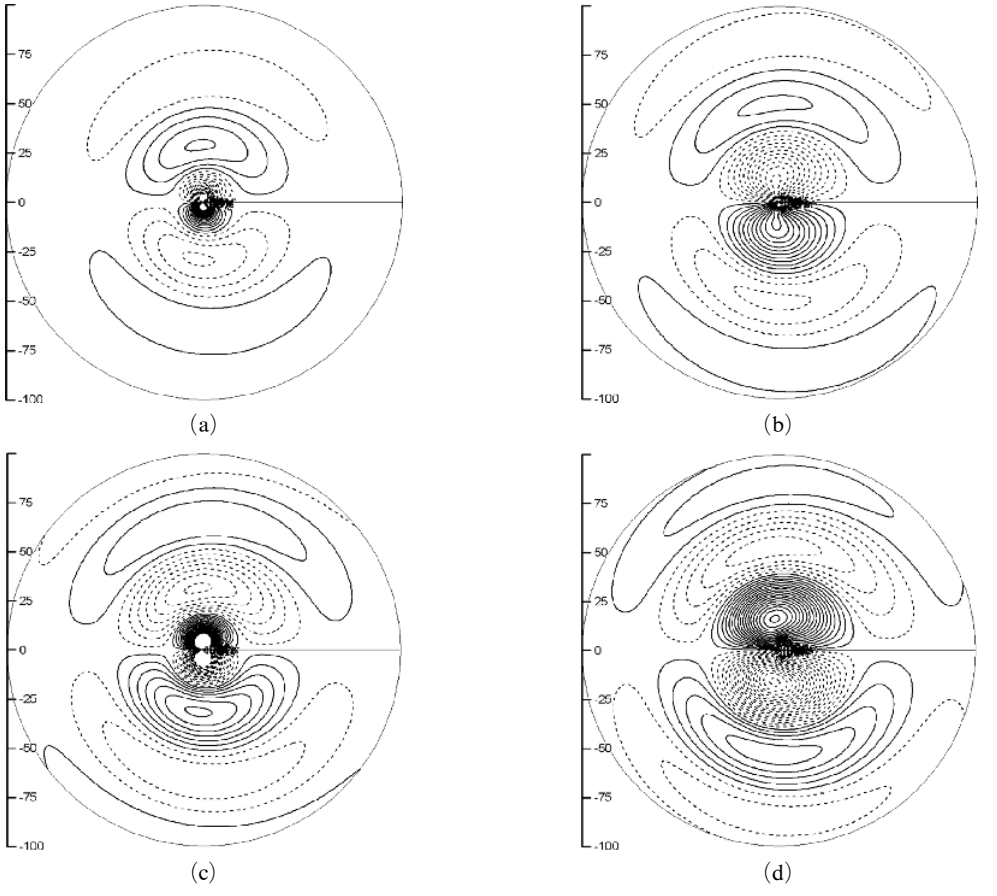

Fig. 12 Instantaneous pressure contours (40 levels from −5.e-4 to 5.e-4) from the ISDM combined with the FLEE: (a) $T=185$, (b) $T=205$, (c) $T=220$ and (d) $T=240$

better agreement with the analytic solution than that of the original ISDM. However, the more distant the ISDM is from the solid surface, the less accurate the CAA solver is for assessing the interaction between the acoustic wave and solid bodies compared with the real situation. Therefore, there needs to be a compromise between the two aspects. Due to the Doppler effects of mean flow, directivity envelopes of both were slightly inclined toward the upstream.

Figure 12 presents the pressure field from the ISDM with the FLEE in which the acoustic waves are seen to propagate preferably from the cylinder along the normal direction of the flow. However, the numerical solutions of the ISDM linked with the FLEE seem to suffer from the unstable solutions as mentioned by Bogey et al.(2002).

Figure 13 shows the time history of the fluctuating pressure, measured at a distance $r=99D$ from the cylinder center. It can be found that the

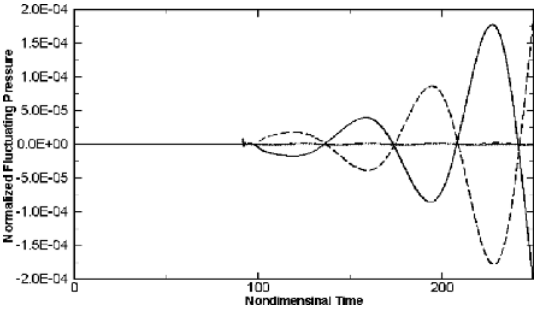

Fig. 13 Fluctuating pressure signal at $r=99D$ of the ISDM with the FLEE ($\theta=0°$ -------, $\theta=90°$ ----, $\theta=180°$ -·-·-·-, and $\theta=270°$ ——)

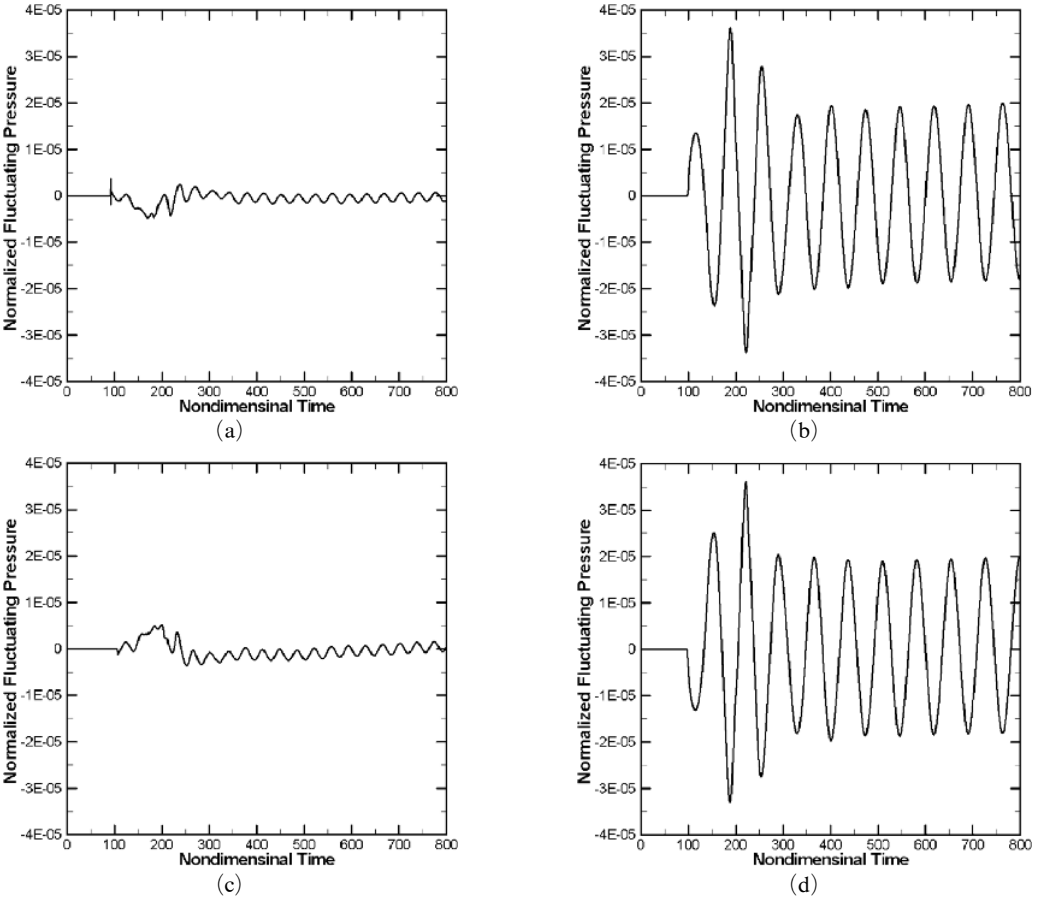

Fig. 14 Fluctuating pressure signal from the ISDM with the NPE measured at $r=99D$ and (a) $\theta=0°$, (b) $\theta=90°$, (c) $\theta=180°$, and (d) $\theta=270°$.

acoustic waves from both are unstable at $\theta=90°$ and 270°.

4.2.3 Acoustic results with NPE

In this section, results of acoustic simulations using the ISDM combined with the NPE are presented.

Figure 14 shows the time history of the fluctuating pressure, calculated at a distance $r=99D$ from the cylinder center at four circumferential positions. Comparing this with the results of the ISDM with the SLEE, no big difference is seen except that the magnitude and the frequency of the oscillating pressure are slightly increased. It is also found that the nonlinear interaction terms suppress the unstable waves which exist in the previous calculation using the FLEE. Using the NPE, however, the oscillating pressure is found to increase in amplitude and frequency. This increase is difficult to interpret. However, conjectures can be proposed. Because the NPE contain non-linear terms allowing for the energy transform between the acoustic and vorticity waves, the generation of noise is ensured both by the source terms issuing from the flow simulation and by the nonlinear perturbation equation itself. These may explain the reason for the increase of the oscillation pressure. It is also well known that nonlinearity causes the wave profile of an acoustic pulse to steepen up and ultimately to form a shock. It was found that the nonlinear wave steepening process, when viewed in the wavenumber domain, corresponded to an energy cascade process whereby low wavenumber components are transferred to high wavenumber range (Tam, 1995). In the absence of shocks, nonlinear effects do not change the net acoustic energy associated with a pulse. They merely cause a rearrangement of the frequency distribution of the energy. From this fact, it can be inferred that the energy cascade process from the nonlinear terms may be responsible for the increase of the oscillating pressure frequency. In other aspect, Seo and Moon (2005) also indicate that excessively generated perturbed vorticity near the wall may yield an unphysical wave. This may be potential reason for the increase of the acoustic pressure in the amplitude and frequency.

5. Numerical Results for Aeolian Tones from Twin Cylinders

In this part, the present numerical methods are applied to the prediction of aeolian tones from twin-cylinders. It is known that the streets of regularly spaced vortices exist with laminar cores over the range of Reynolds numbers from 65 to approximately 400. The range of Reynolds numbers above which vortices with turbulent cores are shed periodically extends to approximately 2×10^5. The strouhal number, which is known to be almost magically constant throughout the subcritical range of Reynolds numbers for the single cylinder, is strongly affected by the interference between the two cylinders and their wakes (Zdravkvich, 1977; 1985; Kiya, 1980). The cylinder configuration concerned in this work is the tandem cylinders separated 3 diameters between centers as shown in Fig. 1. The Reynolds number $Re=1.58\times10^4$ based on inflow velocity $u_\infty=24.5$ m/s and cylinder diameter $D=0.955$ cm are imposed on the computation. This problem is also provided as one of benchmark problems in 4th CAA Workshop (Lee, 2003).

5.1 Numerical results of viscous flow simulations

The viscous flow calculations are carried out on a mesh with approximately 41,103 points in the computational domain. The mesh, and its close-up around the cylinder, is shown in Fig. 15. The mesh for viscous flow simulation consists of

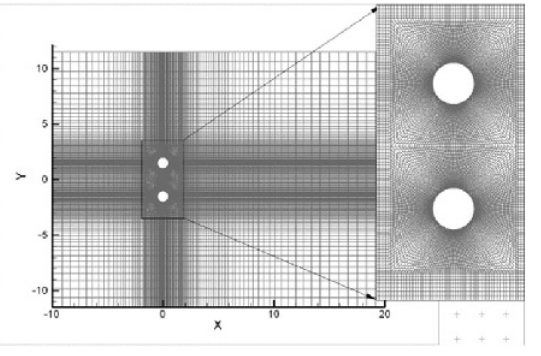

Fig. 15 Mesh for the viscous flow simulation

two types of grids: Inner mesh is the multiply connected grid and outer one is the Cartesian grid. Initially, random disturbances are imposed on a uniform velocity to quickly generate vortex shedding. The computational time step is fixed to be $\Delta t = 0.01/(D/u_\infty)$.

Figure 16 shows the iso-contours of turbulence kinetic energy and pressure at certain time instant. It is evident that anti-phase lift and in-phase drag forces exerted on the cylinder surface fluctuate in time due to the periodic shedding of symmetric vortices. The frequency of vortex shedding can be estimated by evaluating the periodicity of the oscillating lift or drag coefficient.

Time-dependent lift and drag coefficients are presented in Fig. 17, calculated by integrating the distributions of pressure and shear stresses on the cylinder surface. As the computation begins with an initial condition that is given by the flow solutions, vortex shedding does not occur for a considerable time. However, after the first shedding happens, the flow goes through a transient state to arrive at the state of periodic shedding of vortices.

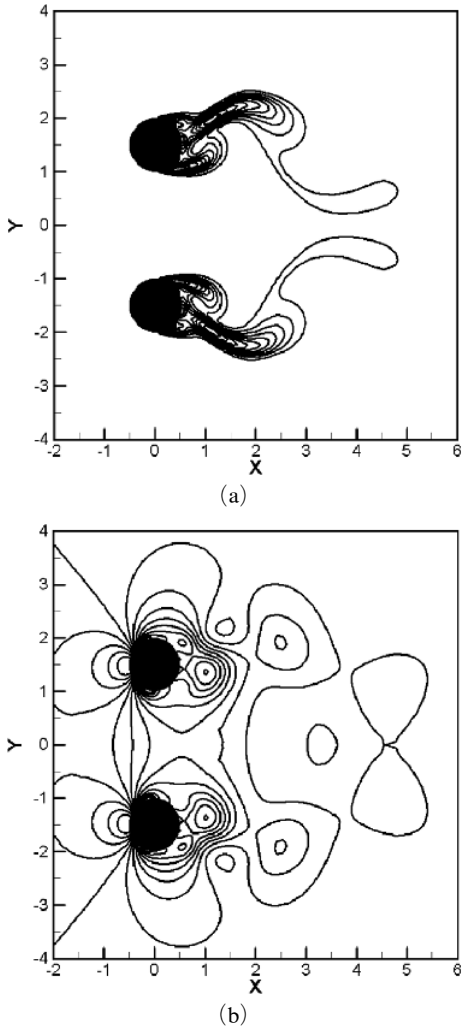

Fig. 16 Instantaneous non-dimensional iso-contours (a) of the turbulence kinetic energy k, 10 levels from 0.1 to 1.0 and (b) of static pressure, 13 levels from −0.8 to 0.4

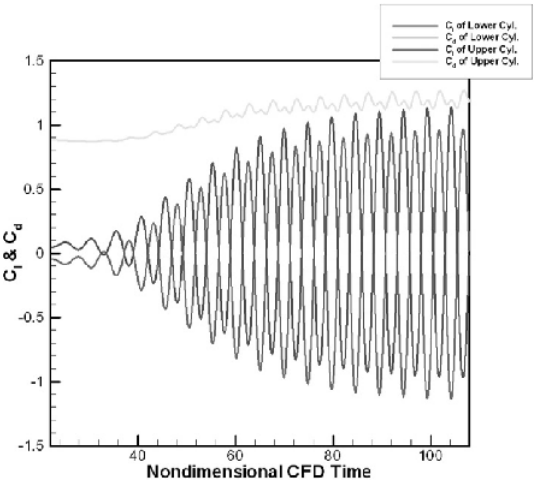

Fig. 17 Time dependent signals of the lift coefficient, C_l and drag coefficient C_d

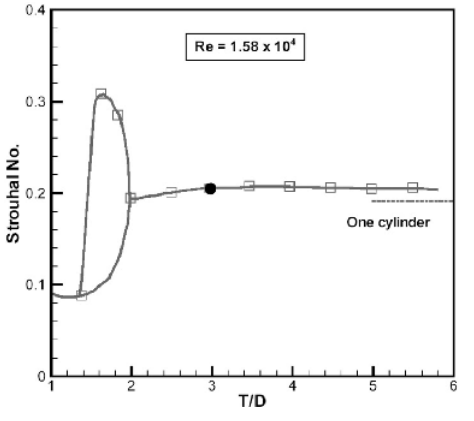

Fig. 18 Comparison of the strouhal number of vortex shedding. (●: present result and □: experimental data from Kia et al., 1980)

Lift and drag coefficients show a sinusoidal variation corresponding to a Strouhal number of 0.2 and 0.4, respectively. This value is in good agreement with the experimental measurement (Kiya, 1980) as shown in Fig. 18.

5.2 Numerical results of acoustic simulations

Non-dimensional period T_f of the vortex shedding is equal to 4.9 with $\Delta t_f=0.01$, which correspond to 490 data points in time. Unsteady hydrodynamic pressure corresponding to a surface dipole sources are recorded on twin-cylinder surface consisting of 101 grid points, respectively. Different time-scale of the acoustic simulation from the viscous flow simulation leads to the different non-dimension period $T_a=68.08$ and numerical time step $\Delta t_a=0.02$, i.e. 3405 data points.

Figure 19 shows the fluctuating pressure, P on the cylinder surface at approximately $0.25T_a$, $0.5T_a$, $0.75T_a$ and T_a, respectively. It can also be found that the fluctuating pressures show symmetric patterns. Fluctuating pressure data are utilized as input data for the construction of the immersed surface dipole model. The numerical results of the viscous flow are transformed onto the grid and time step for acoustic simulation.

The acoustic calculations are performed on a multi-scale overset mesh, which is devised for the analysis for more complex geometry problem such as aeolian tones from twin cylinders. The body-fitted meshes are applied only near the cylinders and multi-scale Cartesian background meshes are applied elsewhere in the domains, as shown in

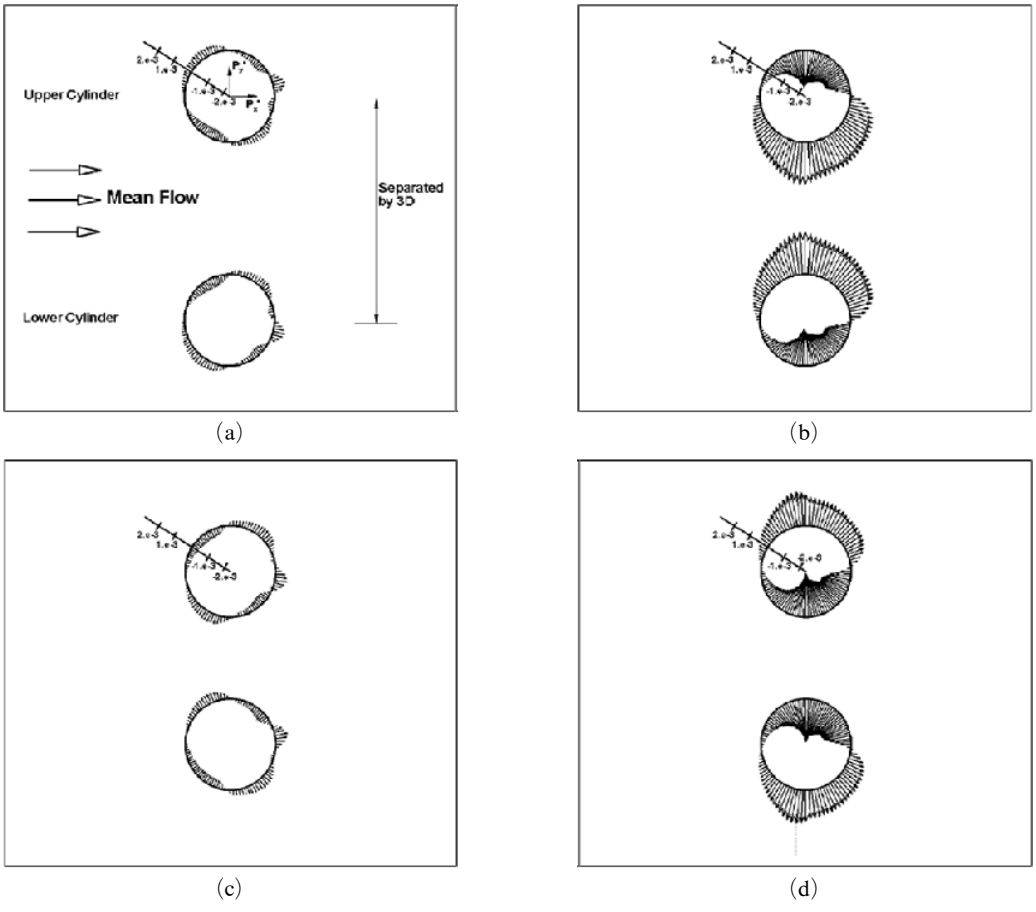

Fig. 19 A sequence of simultaneous surface fluctuating pressure ($P=p-p_0$) at (a) one quarter of a cycle, (b) a half cycle, (c) three quarters of a cycle, (d) the beginning of a cycle

Fig. 20. Full computation domain for the acoustic

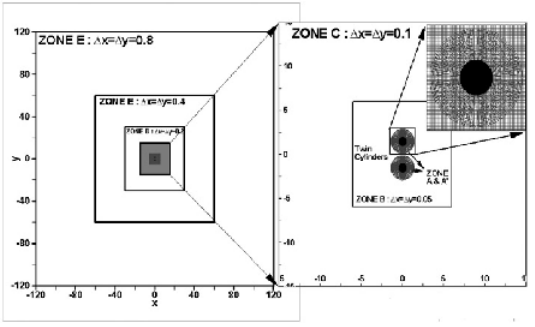

Fig. 20 A sequence of simultaneous surface fluctuating pressure ($P=p-p_0$) at (a) one quarter of a cycle, (b) a half cycle, (c) three quarters of a cycle, (d) the beginning of a cycle

simulations covers the far-field reaching to $120D$, including the far field as well as the near-field. Interpolation algorithm of Bin et al, (2004) is used for the information exchange between the meshes. Based on the previous analysis results on the single cylinder, acoustic calculations are executed with only two approaches: One is the method using only the ISDM in ambient condition and the other uses the ISDM combined with the SLEE.

5.2.1 Acoustic results without mean flow effects

In Fig. 21, fluctuating pressure field obtained from the simulation using the ISDM in ambient condition is plotted during one period. As ex-

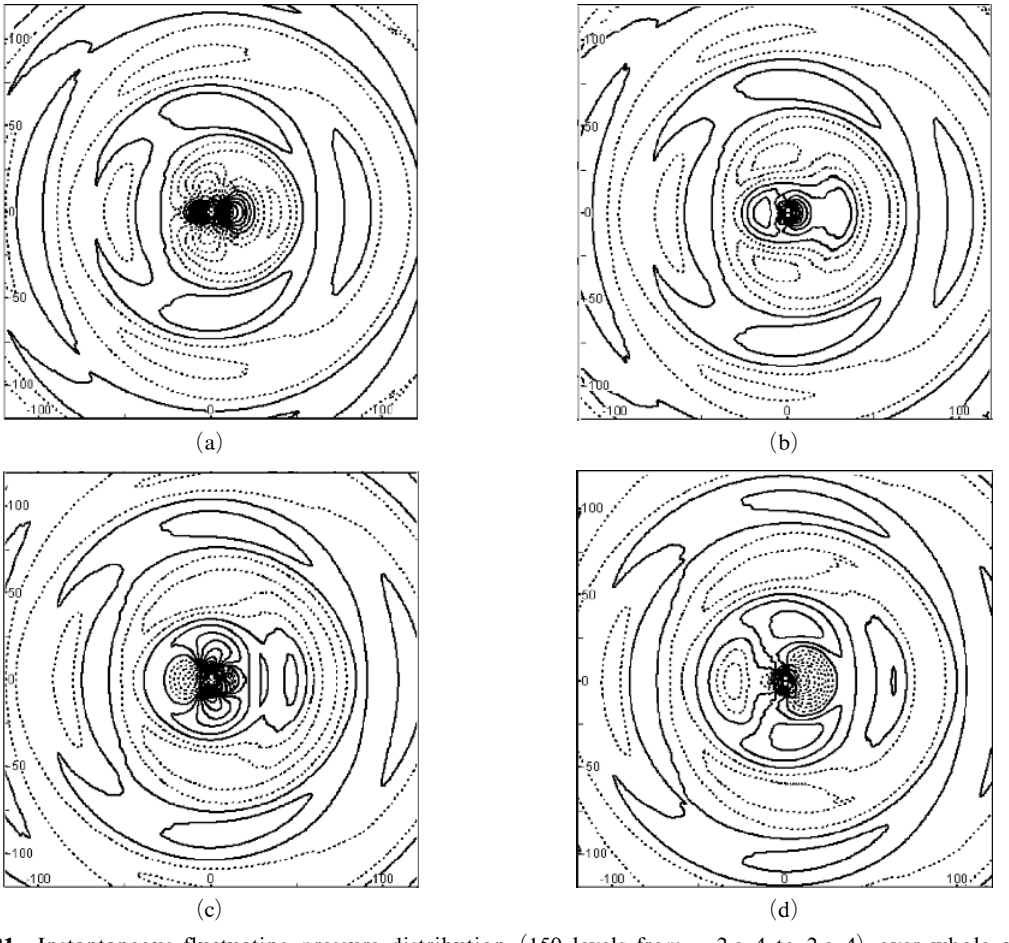

Fig. 21 Instantaneous fluctuating pressure distribution (150 levels from −2.e-4 to 2.e-4) over whole computation domain (a) at $T=155$ (b) at $T=170$, (c) at $T=185$, and (d) at $T=200$

pected, the acoustic waves generated by the lift and drag forces exerted by the cylinder on the flow are mainly propagated in the directions normal and parallel to the mean velocity, respectively.

The directivity patterns of the sound field in the current simulation, measured at $r=10D$ and $r=100D$, are shown in Fig. 22. The results using the ISDM show good agreements with those using point dipole sources. However, the discrepancy is more increased in the $10D$, i.e., the near-field than that in the $100D$, i.e., the far-field. The reason for this may be that the near-field acoustic wave is more affected by the interactions between the acoustic waves and the cylinder surfaces and, the ISDM model can allow for the interactions while the point sources cannot. The amplitudes of the fluctuating pressures by the lift and drag dipole sources are comparable for each other at $r=10D$ while acoustic waves from the lift dipoles are stronger that those from the drag dipoles at $r=100D$. Nevertheless, due to anti-phase of the lift dipoles of twin cylinders, the RMS value of acoustic wave in the direction normal to the mean-

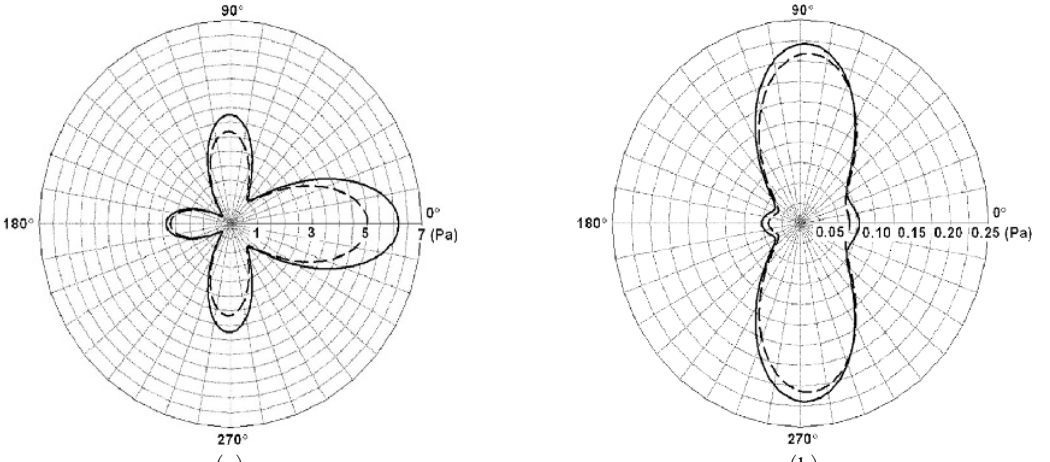

(a) (b)

Fig. 22 Directivity patterns of the mean square value of the fluctuating pressure with out mean flow effects (a) at $r=10D$ and (b) at $r=100D$ (—— ISDM and ---- point dipole sources)

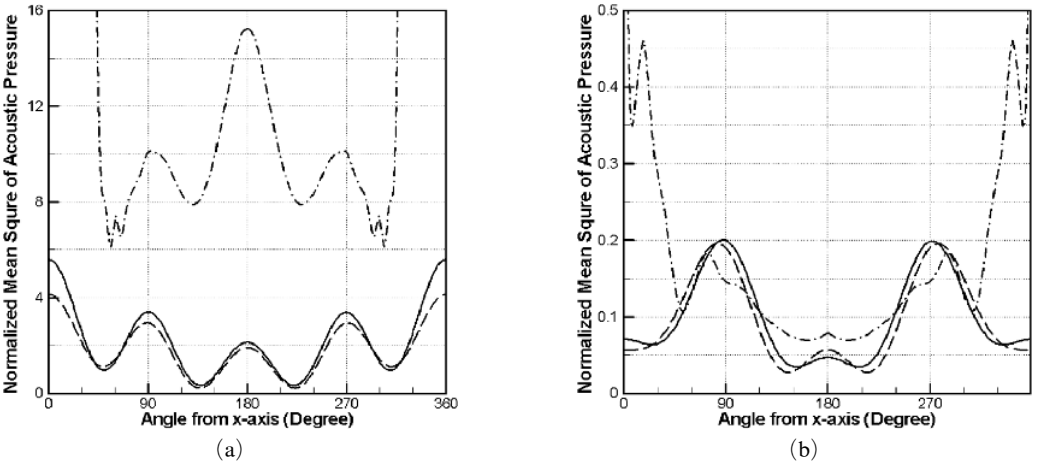

(a) (b)

Fig. 23 Comparison of Normalized Mean Square Acoustic Pressure, Normalized by $S_t \cdot C_{L,RMS}^2$, (a) on $R=10D$ and (b) on $R=100D$. (——: present result, -·-·-·-: Guénanff et al. and ----: Lockard)

flow is five times lower than that of single cylinder.

In order to validate the current numerical approaches, this numerical result is compared with the others using the different numerical techniques, which is shown in Fig. 23. Guénanff et al. (2003) solved the Navier-Stokes equations using the nonlinear disturbance equation and Lockard (2003) used a two-dimensional implementation of the Ffowcs Williams-Hawkings (FW-H) equation to predict the far-field noise. It is observed that the calculated fluctuating forces exerted on the cylinders are somewhat different with one another. These differences also make the variant directivities of acoustic pressure. Therefore, only for the comparison of acoustic computation, the directivities are normalized by $S_t \cdot C_{L,RMS}^2$ to which the mean square value of the acoustic pressure is theoretically known to be proportional in far field. The normalized directivities are shown in Fig. 23(a) and (b). The result of Guénanff et al. (2003) seems to suffer from the "hydrodynamic" pressure fluctuations in the wake. However, the present result shows good agreement with that of Lockhard (2003).

5.2.2 Acoustic results with the LEE

The SLEE combined with the ISDM are utilized for the acoustic simulations of aeolian tone from twin cylinders. Based on the previous result of single cylinder using the SLEE, the surface dipole sources are immersed at the locations $0.1D$ apart from the cylinder surface.

Figure 24 shows the directivity patterns by the ISDM and the point dipole sources. Fig. 24(a) and (b) shows the directivities on the $10D$. It is found that directivity patterns of both are drastically changed especially in the downstream directions, compared with the results without mean flow. This fact emphasizes the effects of mean flow, especially shear layers, on the propagation of acoustic waves. Although the number and direction of the lobes in the directivities are very similar with that using the point dipole sources, the directivity pattern of the ISDM is very different from that, especially in the down-stream direction. This fact emphasizes the role of the dis-

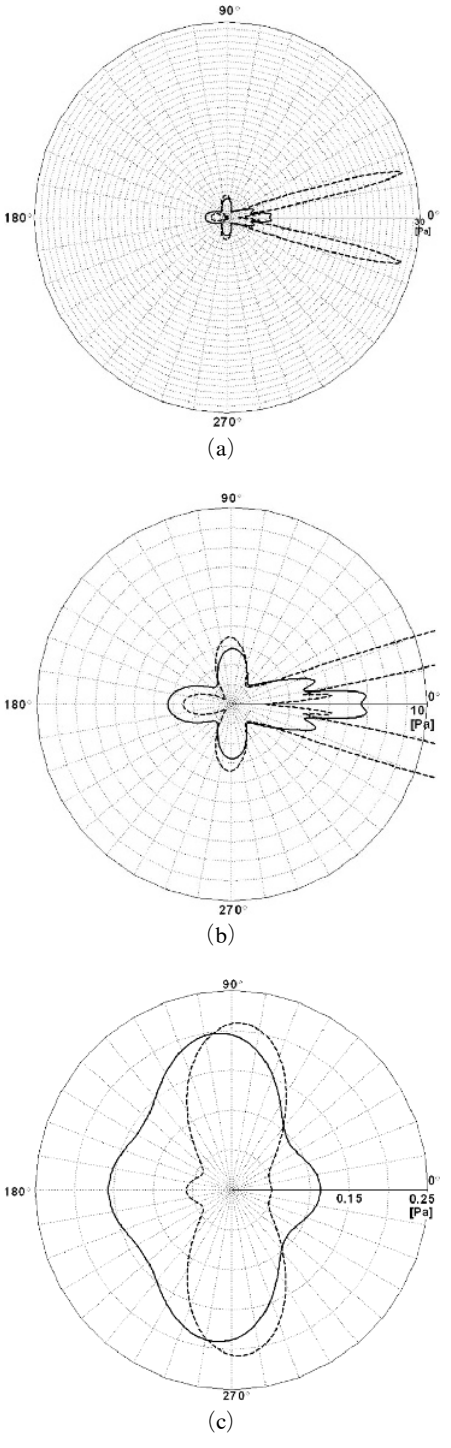

Fig. 24 Directivity patterns of the mean square value of the fluctuating pressure by using the SLEE (a) at $r=10D$, (b) zoomed plot at $r=10D$ and (c) at $r=100D$ (—— ISDM and ---- point dipole sources)

tributed dipole sources on the cylinder surface and its interaction with the cylinder wall in the acoustic wave propagation from twin cylinders. The directivity from the point dipole sources at $r=100D$, shown in Fig. 24(c), shows similar pattern with the result without mean flow effect. However, the directivity from the ISDM with the SLEE is somewhat different from that with ambient condition. Although it is now shown in this paper, the directivity by the ISDM, shown in Fig. 24(c), is similar to that obtained by using the finest grid in the works of Lockhard (2003).

6. Conclusions

The immersed surface dipole model (ISDM) is developed for the efficient computation of aerodynamic noise in low Mach number flow. The immersed surface dipoles are synthesized based on hydrodynamic pressure fluctuations on solid surfaces, which are calculated by using the incompressible aerodynamic simulations. The ISDM combined with various acoustic equations such as simplified linearized Euler equations (SLEE), Full linearized Euler equations (FLEE) and nonlinear perturbation equations (NPE) are applied to the prediction of aeolian tone noise from a circular cylinder in a cross flow. The numerical result using the ISDM without background flow shows a convincing agreement with the analytic result. Based on this result, the ISDM without background flow is recommended for very small Mach number flow, i.e., in the limit $M \rightarrow 0$. The numerical solution of the ISDM with the SLEE shows less RMS values of the fluctuating pressure than that of the ISDM without mean flow. This is due to the energy transfer from the acoustic wave to the vorticity wave on the solid surface. The ISDM with the SLEE has an advantage, compared with that without mean flow, since the interaction of acoustic and mean flow can be allowed for only by making some correction to the ISDM. However, the correction factor, which can be universally applied to the general problems, remains to be achieved. The result of the ISDM with the FLEE is contaminated by the unstable wave. The acoustic solvers using the NPE combined with the ISDM suppress such unstable solutions while generate the more increased pressure fluctuations than the theoretical and previous linear numerical results. Based on the analysis of the numerical results of aeolian tone noise by a single cylinder, the proposed numerical methods using the ISDM in the ambient condition and with the SLEE were applied to the prediction of the Aeolian tone noise from twin cylinders aligned perpendicularly to the mean flow and separated 3 diameters between their centers. The multi-scale overset grids technique was also utilized to resolve the complex geometries of twin cylinders. The symmetric vortices are shed, which leads to the anti-phase of the lift dipoles and the in-phase of the drag dipoles. Due to these phase differences, the directivity of the fluctuating pressure from the lift dipoles shows the comparable magnitude with that from the drag dipoles at 10 diameters apart from the origin. However, the directivity at 100 diameters shows that the lift-dipole originated noise has bigger magnitude than that of the drag-dipole one. Through the comparison with the other numerical results using the different numerical methods, its validity was ensured. Based on these results, it is believed that the current methods can broaden the application area of computational aeroacoustic techniques to practical aeroacoustic phenomena, enhancing both the speed and accuracy of the computation.

Acknowledgments

This work was supported by grant No. R01-2006-000-10301-0 from the Basic Research Program of the Korea Science & Engineering Foundation.

References

Bayliss, A. and Turkel, E., 1982 "Far Field Boundary Conditions for Compressible Flow," *Journal of Computational Physics*, Vol. 48, pp. 182～199.

Bin, J., Cheong, C. and Lee, S., 2004, "Optimized Boundary Treatment of Curved Walls for High-Order Computational Aeroacoustics Schemes,"

AIAA Journal, Vol. 42, No. 2, pp. 414～417.

Blake, W. K. 1986, *Mechanics of Flow-Induced Sound and Vibration*, Academic Press, INC., Vol. 1 pp. 280～283.

Blevins, R. D. and Ressler, M. M., 1993, "Experimentals on Acoustic Resonance in Heat Exchanger Tube Bundles," *Journal of Sound Vibration*, Vol. 164, No. 3, pp. 503～533.

Benhamadouche, S. and Laurence, D., 2003, "LES, Coarse LES, and Transient RANS Comparisons on the Flow Across a tube Bundle," *International Journal of Heat and Fluid Flow*, Vol. 24, pp. 470～479.

Bogey, C., Bailly, C. and Juve, D., 2002, "Computation of Flow Noise Using Source Terms in Linearized Euler's Equations," *AIAA Journal*, Vol. 40, No. 2, pp. 235～2432.

Bouris, D. and Bergeles, G., 1999, "Two Dimensional Time Dependent Simulation of the Subcritical Flow in a Staggered Tube Bundle using a Subgrid Scale Model," *International Journal of Heat and Fluid Flow*, Vol. 20, pp. 105～114.

Cantwell, B. and Coles, C., 1983, "An Experimental Study of Entrainment and Transport in the Turbulent near Wake of a Circular Cylinder," *Journal of Fluid Mechanics*, Vol. 136, pp. 321～374.

Cheong, C. and Lee, S., 2001, "Grid-Optimized Dispersion-Relation-Preserving Schemes on General Geometries for Computational Aeroacoustics," *Journal of Computational Physics*, Vol. 174, pp. 248～276.

Chien, K. Y., 1982, "Prediction of Channel and Boundary Layer Flows with a Low Reynolds Number Turbulence Model," *AIAA Journal*, Vol. 20, pp. 33～38.

Curle, N, 1955, "The Influence of Solid Boundaries Upon Aerodynamic Sound," *Proc. Roy. Soc. Ser. A*, Vol. 231, pp. 505～514.

Ffowcs Williams, J. E. and Hawkings, J. E., 1968, "Sound Generation by Turbulence and Surfaces in Arbitrary Motion," *Philo. Trans. R. Soc. London Series A*, Vol. 264, pp. 321～342.

Goldstein, M. E., 2002, "A Unified Approach to Some Recent Developments in Jet Noise Theory," *International Journal of Aeroacoustics*, Vol. 1, pp. 1～16.

Guénanff, R., Manoha, E., Terracol, M. and Redonnet, S., 2003, "Problem 1 : Aeolian Tone Generation From Two Cylinders," in the Proceeding of 4th CAA Workshop on Benchmark Problems.

Hardin, J. C. and Pope, D. S., 1994, "An Acoustic/Viscous Splitting Technique For Computational Aeroacoustics," *Theoretical Computational Fluid Dynamics*, Vol. 6, pp. 323～340.

Hardin, J. C. and Pope, D. S., 1995, "Sound Generation by Flow over a Two-Dimensional Cavity," *AIAA Journal*, Vol. 33, No. 3, pp. 407～412.

Hobson, G. V. and Lakshiminarayana, B., 1991, "Prediction of Cascade Performance Using an Incompressible Navier-Stokes Technique," *Journal of Turbomachinery*, Vol. 113, pp. 561～572.

Hu, F. Q., Hussaini, M. Y. and Manthey, J. L., 1996 "Low-Dissipation and Low-Dispersion Runge-Kutta schemes for Computational Aeroacoustics," *Journal of Computational Physics*, Vol. 124, pp. 177～191.

Kang, D. J., Bae, S. S. and Joo, S. W., 1998, "An Unstructured FVM for the Numerical Prediction of Incompressible Viscous Flows," *Transactions of the KSME*, Vol. 22, pp. 1410～1421.

Kiya, M., Arie, M., Tamura, H. and Mori, H., 1980, "Vortex Shedding from Two Circular Cylinders in Staggered Arrangement," *Transactions of the ASME*, Vol. 102, pp. 166～173.

Lee, S, 2003, "Cateory 5, Problem 1 : Aeolian Tone Generation from Two Cylinders," in the Proceeding of 4th CAA Workshop on Benchmark Problems.

Lele, S. K., 1997, "Computational Aeroacoustics : A Review," AIAA Paper 97-0018.

Lighthill, M. J., 1952, "On Sound Generated Aerodynamically — I. General Theory," *Proc. Roy. Soc. Ser. A*, Vol. 211, pp. 564～587.

Lockard, D. P., 2003, "A Hybrid Approach to Tandem Cylinder Noise," in the Proceeding of 4th CAA Workshop on Benchmark Problems.

Seo, J. H. and Moon, Y. J., 2005, "Perturbed Compressible Equations for Aeroacoustic Noise Prediction at Low Mach Numbers," *AIAA Journal*, Vol. 43, No. 8. pp. 1716～1724.

Oengoren, A. and Ziada, S., 1998, "An In-

Depth Study of Vortex Shedding, Acoustic Resonance and Turbulent Forces in Normal Triangle Tube Arrays," *Journal of Fluid Structures*, Vol. 12, pp. 717～758.

Rollet-Miet, P., Laurence, D. and Ferziger, J., 1999, "LES and RANS of Turbulent Flow in Tube Bundles," *International Journal of Heat and Fluid Flow*, Vol. 20, pp. 241～254.

Shen, W. Z. and Sorensen, J. N., 1999, "Aeroacoustic Formulation of Low-Speed Flows," *Theoretical Computational Fluid Dynamics*, Vol. 13, pp. 271～289.

Shen, W. Z. and Sorensen, J. N., 2001, "Aeroacoustic Modeling of Turbulent Airfoil Flow," *AIAA Journal*, Vol. 39, No. 6, pp. 1057～1064.

Tam, C. K. W. and Web, J. C., 1993, "Dispersion-Relation-Preserving Schemes for Computational Acoustics," *Journal of Computational Physics*, Vol. 107, pp. 262～281.

Tam, C. K. W. and Shen, H., 1993, "Direct Computation on Nonlinear Acoustic Pulses Using High-Order Finite Difference Schemes," AIAA paper 93-4325.

Tam, C. K. W. and Dong, Z., 1994, "Wall Boundary Conditions for High-Order Finite Difference Schemes for Computational Aeroacoustics," *Theoretical Computational Fluid Dynamics*, Vol. 8, pp. 303～322.

Tam, C. K. W., 1995, "Computational Aeroacoustics : Issues and Methods," *AIAA Journal*, Vol. 33, pp. 1788～1796.

Thomadakis, M. and Leschziner, M., 1996, "A Pressure Correction Method for the Solution of Incompressible Viscous Flows on Unstructured Grids," *International Journal of Numerical Method in Fluids*, Vol. 22, pp. 581～600.

Zdravkovich, M. M., 1977, "Review of Flow Interference Between Two Circular Cylinders in Various Arrangements," *ASME Journal*, Vol. 99, pp. 618～633.

Zdravkovich, M. M., 1985, "Flow Induced Oscillations of Two Interfering Circular Cylinders," *Journal of Sound and Vibration*, Vol. 101, No. 4, pp. 511～521.